



Environmental  
Science  
Nano

**Carbon-titanium dioxide (C/TiO<sub>2</sub>) nanofiber composites for  
chemical oxidation of emerging organic contaminants in  
reactive filtration applications**

Journal:	<i>Environmental Science: Nano</i>
Manuscript ID	EN-ART-09-2020-000975.R1
Article Type:	Paper

SCHOLARONE™  
Manuscripts

### **Environmental Significance Statement**

For water treatment applications, functionalized nanocomposites hold promise for integrating reactive nanoparticles into a stable and scalable platform. Here, we fabricate, optimize and demonstrate the performance of electrospun carbon nanofibers with integrated photocatalytic titanium dioxide for use as reactive filtration materials. We illustrate the viability of these materials for advanced oxidation processes in a flow through filtration system targeting a suite of otherwise recalcitrant constituents of emerging concern in complex matrices representative of source and finished drinking water. We envision that these carbon-titanium dioxide nanofiber filters are ideal for decentralized water treatment (e.g., point of use and entry systems), where versatile, multi-functional technologies are needed to address complex water quality challenges in a small technology footprint.

1  
2  
3  
4  
5  
6  
7  
8  
9  
10  
11 **Carbon-titanium dioxide (C/TiO<sub>2</sub>) nanofiber composites for chemical oxidation of**  
12 **emerging organic contaminants in reactive filtration applications**  
13  
14  
15  
16  
17  
18  
19

20 Katherine E. Greenstein,<sup>1</sup> Matthew R. Nagorzanski,<sup>1</sup> Bailey Kelsay,<sup>1</sup> Edgard M.  
21 Verdugo,<sup>1</sup> Nosang V. Myung,<sup>2</sup> Gene F. Parkin,<sup>1</sup> David M. Cwiertny<sup>1,3\*</sup>  
22  
23  
24  
25  
26  
27  
28  
29

30 <sup>1</sup>Department of Civil and Environmental Engineering, University of Iowa, Iowa City, IA 52242

31 <sup>2</sup>Department of Chemical and Biomolecular Engineering, University of Notre Dame, IN 46556

32 <sup>3</sup>Department of Chemical and Biochemical Engineering, University of Iowa, Iowa City, IA  
33 52242  
34  
35  
36  
37  
38  
39  
40  
41  
42  
43  
44  
45

46 \*Corresponding Author Contact Information:

47 David M. Cwiertny

48 Address: 4105 Seamans Center

49 University of Iowa, Iowa City, IA 52242

50 E-mail: david-cwiertny@uiowa.edu

51 Phone: 319-335-1401  
52  
53  
54  
55  
56  
57  
58  
59  
60

Fax: 319-335-5660

Revised manuscript submitted to: *Environmental Science: Nano*

January 31, 2021

### ABSTRACT

The recalcitrance of some emerging organic contaminants through conventional water treatment systems may necessitate advanced technologies that use highly reactive, non-specific hydroxyl radical. Here, polyacrylonitrile (PAN) nanofibers with embedded titanium dioxide (TiO<sub>2</sub>) nanoparticles were synthesized via electrospinning and subsequently carbonized to produce mechanically stable carbon/TiO<sub>2</sub> (C/TiO<sub>2</sub>) nanofiber composite filters. Nanofiber composites were optimized for reactivity in flow through treatment systems by varying their mass loading of TiO<sub>2</sub>, adding phthalic acid (PTA) as a dispersing agent for nanoparticles in electrospinning sol gels, comparing different types of commercially available TiO<sub>2</sub> nanoparticles (Aeroxide® P25 and 5 nm anatase nanoparticles) and through functionalization with gold (Au/TiO<sub>2</sub>) as a co-catalyst. High bulk and surface TiO<sub>2</sub> concentrations correspond with enhanced nanofiber reactivity, while PTA as a dispersant makes it possible to fabricate materials at very high P25 loadings (~80% wt.%). The optimal composite formulation (50 wt.% P25 with 2.5 wt.% PTA) combining high reactivity and material stability was then tested across a range of variables relevant to filtration applications including filter thickness (300-1,800 μm), permeate flux (from 540-2700 L/m<sup>2</sup>-h), incident light energy (UV-254 and simulated sunlight), flow configuration (dead-end and cross-flow filtration), presence of potentially interfering co-solutes (dissolved organic matter and carbonate alkalinity),

1  
2  
3 and across a suite of eight organic micropollutants (atrazine, benzotriazole, caffeine,  
4 carbamazepine, DEET, metoprolol, naproxen, and sulfamethoxazole). During cross-flow  
5 recirculation under UV-irradiation, 300  $\mu\text{m}$  thick filters (30 mg total mass) produced  
6 micropollutant half-lives  $\sim 45$  min, with 40-90% removal (from an initial 0.5  $\mu\text{M}$  concentration) in  
7 a single pass through the filter. The initial reaction rate coefficients of micropollutant  
8 transformation did not clearly correlate with reported second order rate coefficients for reaction  
9 with hydroxyl radical ( $k_{\text{OH}}$ ), implying that processes other than reaction with photogenerated  
10 hydroxyl radical (e.g., surface sorption) may control the overall rate of transformation. The  
11 materials developed herein represent a promising next-generation filtration technology that  
12 integrates photocatalytic activity in a robust platform for nanomaterial-enabled water treatment.  
13  
14  
15  
16  
17  
18  
19  
20  
21

22 **Keywords:** electrospinning, water treatment, environmental nanotechnology, photocatalysis,  
23 emerging contaminants  
24  
25  
26  
27  
28  
29  
30  
31  
32  
33  
34  
35  
36  
37  
38  
39  
40  
41  
42  
43  
44  
45  
46  
47  
48  
49  
50  
51  
52  
53  
54  
55  
56  
57  
58  
59  
60

## 1. INTRODUCTION

To address more recalcitrant pollutant classes, the use of titanium dioxide (TiO<sub>2</sub>) as a photocatalyst for advanced oxidation processes (AOPs) remains widely studied<sup>1-3</sup> despite well-recognized barriers to its practical implementation.<sup>4-6</sup> Because commercially available nanoparticle catalysts (i.e., Aeroxide® P25) can be challenging to deploy as dispersions at water treatment scale, we recently explored the potential of using three-dimensional networks of TiO<sub>2</sub> nanofibers fabricated via electrospinning<sup>7</sup> as an alternative platform for coupling chemical oxidation processes for dissolved micropollutants with filtration (i.e., removal of suspended particles via physical capture within the nanofiber network).<sup>8</sup> Unfortunately, we,<sup>7</sup> and others,<sup>9</sup> have found nanofibers of pure TiO<sub>2</sub> to be brittle and thus not practically viable as a stand-alone platform when compared with more robust polymeric<sup>10</sup> or even carbon nanofibers (CNFs)<sup>11</sup> generated via electrospinning.

To develop a cohesive electrospun platform that balances material strength and reactivity, recent studies have explored the immobilization of TiO<sub>2</sub> nanoparticles on or within polymeric electrospun nanofibers [e.g., cellulose or polyacrylonitrile (PAN)].<sup>12</sup> Several synthesis approaches are common, including (i) direct addition of TiO<sub>2</sub> nanoparticles or nanorods into electrospinning precursor solutions;<sup>13-15</sup> (ii) incorporation of Ti-containing compounds (e.g., titanium tetraisopropoxide) into electrospinning precursor solutions with post-processing to form *in situ* TiO<sub>2</sub> nanoparticles;<sup>16-19</sup> and (iii) hydrothermal treatment of previously fabricated nanofibers for TiO<sub>2</sub> surface deposition.<sup>20-22</sup> Many of these have been fabricated for applications beyond water treatment, including air purification<sup>21, 23-24</sup> and oil-water separation.<sup>25</sup>

Of those most relevant to technology development for water treatment, the majority have focused on treatment targets (e.g., dyes) of limited relevance to the current challenges of water

1  
2  
3 treatment providers resulting from emerging pollutant classes.<sup>15,22</sup> In one noteworthy study, PVDF  
4 nanofibers electrospayed with TiO<sub>2</sub> nanoparticles were used for oxidation of bisphenol A, 4-  
5 chlorophenol, and cimetidine.<sup>26</sup> However, the multiple synthesis steps required and concern over  
6 stability of surface deposited TiO<sub>2</sub> (as opposed to TiO<sub>2</sub> integrated into nanofibers) may still limit  
7 the viability of such composite materials for water treatment. In another report, PAN nanofibers  
8 containing a Ti precursor were treated hydrothermally to grow TiO<sub>2</sub> *in situ* and then demonstrated  
9 for oxidation of phenol, a model hydroxyl radical probe compound.<sup>19</sup> However, PAN, which  
10 contains electron rich nitrile groups, likely scavenged some of the hydroxyl radical species,  
11 reducing treatment efficiency.<sup>19</sup> In addition, although PVDF is expected to withstand the oxidants  
12 generated by TiO<sub>2</sub>/UV, many polymers, including PAN, are not similarly resistant to oxidation.<sup>27</sup>  
13  
14  
15  
16  
17  
18  
19  
20  
21  
22  
23  
24  
25

26 Carbon is likely a more promising material for a TiO<sub>2</sub> composite; it can withstand the  
27 oxidative environment created by TiO<sub>2</sub>/UV and it may also function as sorbent that can concentrate  
28 some organic targets for subsequent degradation by photogenerated hydroxyl radicals ( $\bullet$ OH) likely  
29 to be most concentrated at the composite surface. Nevertheless, development and performance  
30 assessments of carbon/TiO<sub>2</sub> nanofiber composites remain sparse and have thus far primarily  
31 centered on hydrothermal growth or solvothermal synthesis of TiO<sub>2</sub> nanostructures on pre-  
32 fabricated electrospun CNFs.<sup>28-29</sup> These syntheses demand post-processing of electrospun and  
33 stabilized/carbonized nanofibers, which adds to the complexity and time required for making  
34 materials. Further, CNFs can also suffer from being as brittle and low in material strength as most,  
35 pure inorganic nanofibers, which leaves their viability as reactive water filtration platforms in  
36 question. Indeed, several reactivity studies with carbon/TiO<sub>2</sub> reactivity have been conducted in  
37 batch suspensions after breaking up (i.e., dispersing) the carbon/TiO<sub>2</sub> nanofibers (as we previously  
38 did for pure TiO<sub>2</sub> nanofibers),<sup>7</sup> thereby neglecting any consideration of material strength during  
39  
40  
41  
42  
43  
44  
45  
46  
47  
48  
49  
50  
51  
52  
53  
54  
55  
56  
57  
58  
59  
60

1  
2  
3 composite development.<sup>28-29</sup> It is worth noting, that as with polymer composites, most of this work  
4  
5 with carbon-based composites has yet to demonstrate nanofiber performance in conditions  
6  
7 representative of water treatment, often focusing on photocatalytic removal of dyes (e.g.,  
8  
9 methylene blue, methyl orange, and acid red) at relatively high (5-15 mg/L) concentrations.<sup>28-29</sup>  
10  
11

12         Herein, we develop a TiO<sub>2</sub>-based nanofiber composite via an electrospinning synthesis that  
13  
14 (i) is simplified (i.e., single-pot); (ii) improves material strength, durability and flexibility relative  
15  
16 to pure TiO<sub>2</sub> nanofibers; and (iii) enables photocatalytic reactivity in a flow through platform able  
17  
18 to target the most persistent organic micropollutants during conventional water treatment. We use  
19  
20 a single-pot electrospinning method to produce polyacrylonitrile (PAN) nanofibers with embedded  
21  
22 Aeroxide® P25 nanoparticles (a commercially available TiO<sub>2</sub> photocatalyst with bandgap of 3.2  
23  
24 eV, corresponding to an excitation wavelength of ~390 nm),<sup>30</sup> where subsequent  
25  
26 stabilization/carbonization is used to convert PAN into a flexible and photochemically active  
27  
28 carbon/titanium dioxide (C/TiO<sub>2</sub>) composite. Using this approach, we demonstrate the ability to  
29  
30 electrospin PAN/TiO<sub>2</sub> composites with up to 80 wt% TiO<sub>2</sub> relative to PAN with aid of an organic  
31  
32 acid dispersant, phthalic acid, producing a nanofiber framework mostly comprised of TiO<sub>2</sub> but that  
33  
34 still retains some strength and flexibility derived from its PAN, and ultimately carbon, backbone.  
35  
36  
37  
38  
39

40         For a suite of systematically tailored C/TiO<sub>2</sub> composites, we assessed and optimized the  
41  
42 nanofiber properties most influential on material photocatalytic activity toward atrazine, a widely  
43  
44 applied organic herbicide and regulated contaminant in drinking water. Composite variables  
45  
46 explored included (i) mass loading of TiO<sub>2</sub>; (ii) concentration of phthalic acid incorporated into  
47  
48 electrospinning precursor solutions; and (iii) the type and size of TiO<sub>2</sub> nanoparticles [e.g., mixed-  
49  
50 phase Aeroxide® P25 with ~21 nm diameter, 5 nm anatase TiO<sub>2</sub> nanoparticles, and P25 with  
51  
52 deposited gold as a co-catalyst (Au/TiO<sub>2</sub>)]. All reactivity studies toward atrazine were conducted  
53  
54  
55  
56  
57  
58  
59  
60



1  
2  
3 in a cross-flow UV microfiltration apparatus, and thus we also explored how process flow rate and  
4 the thickness of the photoactive composite nanofiber network (tailored by the volume of  
5 electrospinning precursor used in fabrication) influenced atrazine removal efficiencies. Ultimately,  
6 the performance of the optimal C/TiO<sub>2</sub> composite was tested toward a suite of organic  
7 micropollutants frequently detected in drinking water that are recalcitrant to conventional  
8 treatment,<sup>31-33</sup> including benzotriazole, carbamazepine, DEET, metoprolol, and sulfamethoxazole,  
9 and in matrices representative of water treatment, revealing these composite filters to be a  
10 promising hybrid filtration-advanced oxidation process for water treatment.  
11  
12  
13  
14  
15  
16  
17  
18  
19  
20  
21  
22  
23

## 24 **2. EXPERIMENTAL METHODS**

### 25 *2.1. Reagents*

26 A complete list of reagents can be found in the Electronic Supporting Information (ESI).  
27  
28

### 29 *2.2. Synthesis of C/TiO<sub>2</sub> composites*

30  
31 PAN nanofibers containing phthalic acid (PTA) and seeded with TiO<sub>2</sub> nanoparticles were  
32 electrospun, stabilized, and carbonized to obtain C/TiO<sub>2</sub> composite nanofiber filters. Nanofibers  
33 were prepared to assess the impact of TiO<sub>2</sub> nanoparticle size, phase composition, and mass loading  
34 in CNFs, as well as the impact of PTA (both as a dispersant for TiO<sub>2</sub> in sol gels and to introduce  
35 nanofiber porosity)<sup>11</sup> on C/TiO<sub>2</sub> composite flexibility and reactivity. Either 5 nm TiO<sub>2</sub> (anatase)  
36 or Aeroxide® P25 (~75%:25% anatase: rutile; ~21 nm in diameter) nanoparticles were suspended  
37 in DMF (from 1 to 7 mL) with either no PTA or 2.5 wt.% PTA (relative to total sol gel mass) and  
38 sonicated for 5 h. PAN (8 wt.% relative to DMF) was added and dissolved by thermally mixing  
39 the solution at 60 °C for 2 h. For assessment of TiO<sub>2</sub> mass loading of P25 on reactivity, 15 to 80  
40 wt.% P25 was added to sol gels along with 2.5 wt.% PTA. To evaluate the effect of PTA, sol gels  
41 with either 50 wt.% P25 or 50 wt.% 5 nm TiO<sub>2</sub> were prepared both free of PTA and with 2.5 wt.%  
42  
43  
44  
45  
46  
47  
48  
49  
50  
51  
52  
53  
54  
55  
56  
57  
58  
59  
60

1  
2  
3 PTA. These sol gels were also used to compare the effect of TiO<sub>2</sub> nanoparticle size and phase on  
4 composite reactivity. Finally, because noble metals co-catalyst can improve TiO<sub>2</sub> photocatalytic  
5 performance,<sup>7</sup> a subset of composites were prepared using gold-functionalized P25 particles (i.e.,  
6 Au/TiO<sub>2</sub>) that were prepared via the dropwise reduction of 1 mM Au(III) chloride with 10 mM  
7 ascorbic acid in a suspension of P25 nanoparticles (2 g/L with 150 mL total volume; full  
8 synthesis details are in the ESI). Assuming complete deposition, this would produce an Au  
9 loading of 1.5 wt%. In our prior work,<sup>7</sup> we used a similar method with urea as the reductant to  
10 deposit ~2-5 nm Au nanoparticles on TiO<sub>2</sub>.  
11  
12  
13  
14  
15  
16  
17  
18  
19  
20  
21  
22  
23

24 After cooling to room temperature following thermal mixing, prepared sol gels were  
25 electrospun with a 23G needle and 15 kV/10 cm with a flow rate of 0.5 mL/h using a previously  
26 described system.<sup>11</sup> The electrospinning process was ceased after 6 h, and the mat was peeled off  
27 the Al foil-coated grounded collector. Electrospun PAN/TiO<sub>2</sub> nanofibers were then stabilized at  
28 250 °C in air for 2.5 h and carbonized at 450 °C in nitrogen (N<sub>2</sub>) for 1 h in a tube furnace (MTI  
29 OTF 1200x) (with ramp rate of 5°C/min). This relatively low annealing temperature was used to  
30 produce an amorphous carbon likely to exhibit mechanical properties (e.g., flexibility, not brittle)  
31 necessary for use in water filtration applications. After stabilization and carbonization, nanofiber  
32 mats were cut into circles with diameter of 47 mm for use in reactive filtration experiments.  
33  
34  
35  
36  
37  
38  
39  
40  
41  
42  
43  
44

### 45 *2.3. Nanofiber filter characterization*

46 C/TiO<sub>2</sub> nanofiber composites were characterized to ascertain their chemical and physical  
47 properties. Filter thickness and nanofiber diameter were quantified with a Hitachi S-4800 scanning  
48 electron microscope (SEM) as in our prior work.<sup>7</sup> Briefly, filter thickness was determined by cross-  
49 sectional imaging of C/TiO<sub>2</sub> mats, whereas the average nanofiber diameter within a filter was  
50 determined from measurement of at least 100 nanofibers. In both cases, dimensions in SEM images  
51  
52  
53  
54  
55  
56  
57  
58  
59  
60

1  
2  
3 were sized using the software program ImageJ. SEM imaging was also used to evaluate the TiO<sub>2</sub>  
4 abundance and distribution in all C/TiO<sub>2</sub> materials, as well as the presence or absence of pores  
5 introduced by PTA. The phase of TiO<sub>2</sub> nanoparticles embedded in composites was confirmed with  
6 X-ray diffraction (XRD, Rigaku MiniFlexII, Co X-ray source). N<sub>2</sub>-BET analysis (Quantachrome  
7 Nova 4200e) was used to determine surface area of nanofiber composites after outgassing samples  
8 at 60°C for 6 h prior to measurement. Due to the amount of material consumed during N<sub>2</sub>-BET  
9 measurements, we only conducted single analyses on select, high priority samples. Relative  
10 abundance of Ti on the surface of nanofibers was analyzed with a Kratos Axis Ultra X-ray  
11 photoelectron spectroscopy (XPS) system equipped with a monochromatic Al K $\alpha$  X-ray  
12 source. Additional details related to sample preparation for material characterization are  
13 provided in the ESI.  
14  
15  
16  
17  
18  
19  
20  
21  
22  
23  
24  
25  
26  
27  
28  
29  
30  
31  
32

#### 33 *2.4. Photocatalytic Filtration Experiments*

34  
35 Composite nanofiber filter performance was assessed in a custom-built cross-flow filtration  
36 apparatus with integrated quartz window to allow UV or simulated sunlight irradiation during  
37 operation. A 47 mm diameter nanofiber filter was supported with a 0.22  $\mu$ m PVDF filter  
38 (Durapore) and placed into a Millipore filter holder modified with a 38 mm diameter quartz  
39 window (see schematic in **Figure S1**). During photocatalytic filtration experiments, the quartz  
40 window was exposed to UV light from an Hg(Xe) arc lamp (Newport, 200W) with a 250 nm cut-  
41 on long-pass filter (Asahi Spectra) or a 305 nm cut-on long-pass filter (for a limited number of  
42 experiments simulating sunlight). The spectral irradiance of this source is shown in **Figure S2**.  
43  
44  
45  
46  
47  
48  
49  
50  
51  
52  
53  
54  
55  
56  
57  
58  
59  
60

1  
2  
3 The majority of experiments was conducted with 500 mL of test solution prepared using 5  
4 mM phosphate buffer adjusted to pH 7 spiked with 0.14 (30  $\mu\text{g/L}$  or 10-times the US EPA  
5  
6 Maximum Contaminant Limit or MCL), 0.5 or 2  $\mu\text{M}$  of atrazine. Experiments were also conducted  
7  
8 with 0.5  $\mu\text{M}$  of benzotriazole, caffeine, carbamazepine, DEET, metoprolol, naproxen or  
9  
10 sulfamethoxazole. We note that all micropollutant test solutions were prepared from saturated  
11  
12 aqueous stocks as described in the ESI. Additional trials were conducted with atrazine in matrices  
13  
14 more representative of environmental samples including model humic acid (up to 10 mg/L of Fluka  
15  
16 Humic Acid) and alkalinity (5 mM carbonate).  
17  
18  
19  
20

21  
22 Cross-flow filtration experiments with light irradiation were conducted for up to 3 h, during  
23  
24 which 0.5 mL samples were taken periodically from the feed reservoir, retentate (i.e., the cross-  
25  
26 flow effluent that did not pass through the filter), and permeate (i.e., the through-flow effluent that  
27  
28 had passed through the filter) (see **Figure S1**). Solutions were pumped across and through the filter  
29  
30 at equal rates, from 10 mL/min across and 10 mL/min through (540  $\text{L/m}^2/\text{h}$  flux; within the range  
31  
32 typical for microfiltration) up to 50 mL/min across and 50 mL/min through (2,700  $\text{L/m}^2/\text{h}$  flux).  
33  
34 Flow rates were measured volumetrically (from the volume collected in a 10 mL graduated  
35  
36 cylinder over 30 seconds) and controlled by adjusting the peristaltic pumping rate and a valve that  
37  
38 regulated the amount of flow across and through the filter. Most experiments were operated with  
39  
40 recirculation, where both filter permeate and retentate were returned to the magnetically stirred  
41  
42 feed reservoir. A small subset of experiments with atrazine was also conducted without any  
43  
44 recirculation, thereby allowing performance comparison of the filter when operating in a single  
45  
46 pass or “dead end” filtration mode.  
47  
48  
49  
50

51  
52 Prior to initiating all photocatalytic experiments, the solution was first circulated through  
53  
54 the filter for 1 h in darkness to allow any sorption of the target analyte on the filter to reach  
55  
56  
57  
58  
59  
60

1  
2  
3 equilibrium. UV and simulated sunlight control experiments were also conducted, in which the  
4 system was operated and sampled without a C/TiO<sub>2</sub> filter to quantify transformation of organic  
5  
6  
7  
8  
9 contaminant targets by direct photolysis.

## 10 2.5. Analytical Methods

11  
12 Samples were analyzed via high performance liquid chromatography with diode array  
13  
14  
15  
16  
17  
18  
19  
20  
21  
22  
23  
24  
25  
26  
27  
28  
29  
30  
31  
32  
33  
34  
35  
36  
37  
38  
39  
40  
41  
42  
43  
44  
45  
46  
47  
48  
49  
50  
51  
52  
53  
54  
55  
56  
57  
58  
59  
60  
Additional HPLC method details are provided in the ESI.

## 3. RESULTS AND DISCUSSION

### 3.1. Composite nanofiber characterization

#### 3.1.1. Physical properties with varying mass loadings of TiO<sub>2</sub>

11  
12  
13  
14  
15  
16  
17  
18  
19  
20  
21  
22  
23  
24  
25  
26  
27  
28  
29  
30  
31  
32  
33  
34  
35  
36  
37  
38  
39  
40  
41  
42  
43  
44  
45  
46  
47  
48  
49  
50  
51  
52  
53  
54  
55  
56  
57  
58  
59  
60  
**Figure 1** shows SEM images and histograms for C/TiO<sub>2</sub> composites with up to 63 wt.% P25 (relative to PAN), denoted as C-(wt.%) hereafter (e.g., C-15 represents CNFs with 15 wt.% P25). Each sol gel also contained 2.5 wt.% PTA (the effects of which will be discussed in further detail below). Histograms of nanofiber diameter distributions reveal that below 33 wt.%, the average diameter of C/TiO<sub>2</sub> nanofibers were roughly constant. In contrast, at higher P25 loadings average nanofiber diameter increased from ~200 nm to 360 ± 80 nm (at 63 wt.% P25; see **Figure 1** and **Figure S3a**), suggesting there is a critical P25 mass above which the composite nanofiber morphology deviates from pure carbon nanofibers (or CNFs).

SEM images also revealed considerable differences in surface morphology of the nanofibers as P25 loading increased. Below C-33 (see **Figure 1a-c**), the nanofibers appear to be predominantly carbon containing isolated aggregates of P25 nanoparticles (~400 nm in diameter), the number of which increases with P25 loading. Above C-33, more aggregates of P25 were observed on the surface of nanofibers, causing them to become visibly rougher. This transition

1  
2  
3 from (primarily) isolated P25 aggregates in CNFs to more evenly distributed P25 aggregates likely  
4  
5 contributes to the increase in diameter observed for these composites.  
6

7  
8 We note that the highest loading of P25 that could be electrospun was 80 wt.% relative to  
9  
10 PAN, and the resulting C-80 nanofibers are shown in **Figure S3b-c**. These nanofibers exhibited  
11  
12 the most dramatic increase in diameter, with most measuring at  $\sim 1 \mu\text{m}$ . However, while  
13  
14 composites with up to 67 wt.% P25 remained moderately flexible based on routinely handling  
15  
16 (e.g., bending and flexing), higher P25 loadings (75 and 80 wt.% P25) were especially brittle,  
17  
18 chalky, and more susceptible to breaking while handling. Thus, they were not extensively utilized  
19  
20 in subsequent flow-through reactivity studies because of concerns over their durability and  
21  
22 likelihood to leach loosely bound P25 during application.  
23  
24  
25

26  
27 Analysis via XPS indicated just 0.3 atomic % (at.%) Ti on the surface of C-15 nanofibers.  
28  
29 Surface Ti concentration increased, albeit non-linearly, with increasing P25 content (**Figure 2a**),  
30  
31 with a more marked increase above 63 wt.%. Specifically, surface Ti concentration more than  
32  
33 doubled (from  $\sim 4$  to  $\sim 9$  at.% Ti) over only a  $\sim 20$  wt.% increase in P25 content for C-63 and C-80  
34  
35 nanofibers. XPS suggests, therefore, that at low mass loadings the majority of P25 appears  
36  
37 embedded within the bulk of the CNFs, and only at higher mass loadings (i.e., above a 63 wt.%)  
38  
39 can more proportional increases in surface Ti be achieved via this synthesis approach.  
40  
41

42  
43 Increases in P25 content also yielded composites with greater specific surface area, as  
44  
45 measured by  $\text{N}_2$  BET isotherms (measured surface areas are reported in **Figure 2b**). While CNFs  
46  
47 without P25 (i.e., C-0) had rather low specific surface area ( $5 \text{ m}^2/\text{g}$ ), the addition of P25 produced  
48  
49 a linear increase in surface area for composites from 33 to 80 wt.%. Thus, despite the  
50  
51 corresponding increase in nanofiber diameter observed for these composites, the roughness  
52  
53 imparted by the accumulation of P25 and P25 aggregates on the nanofiber surface yields  
54  
55  
56  
57  
58  
59  
60

1  
2  
3 considerable increases in composite surface area. Indeed, at the highest loadings investigated (C-  
4 80), as much as a 10-fold increase in surface area (to 50 m<sup>2</sup>/g) relative to C-0 was observed, a  
5  
6 value roughly equivalent to the specific surface area we measured for P25 nanoparticles.  
7  
8  
9

10 Finally, XRD confirmed that the crystal structure of the embedded TiO<sub>2</sub> nanoparticles was  
11 not altered during nanofiber synthesis. **Figure S4** compares X-ray diffraction patterns for P25  
12 nanoparticles and 5 nm TiO<sub>2</sub> nanoparticles to that of their composites. As expected from our prior  
13 work, X-ray diffraction patterns for P25 indicate a mixed phase consisting of both 75% anatase  
14 and 25% rutile, as expected.<sup>7</sup> In contrast, XRD results with 5 nm TiO<sub>2</sub> particles are indicative of  
15 pure anatase, while also showing the line broadening expected for smaller primary particle sizes  
16 (composites prepared from these 5 nm particles are discussed in the ESI, with corresponding SEM  
17 images and histograms in **Figure S5**). In all C/TiO<sub>2</sub> composites, the XRD patterns were consistent  
18 with those obtained with respective TiO<sub>2</sub> starting materials, indicating that the carbonization step  
19 did not alter the phase of TiO<sub>2</sub> within the nanofibers.  
20  
21  
22  
23  
24  
25  
26  
27  
28  
29  
30  
31  
32

### 33 3.1.2. Structural benefits from inclusion of phthalic acid

34

35 The inclusion of 2.5 wt.% PTA increased the average nanofiber diameter of C-50 from 180  
36 ± 40 nm to 310 ± 60 nm (**Figure 3a-b**), presumably due to the increase in precursor solution  
37 viscosity arising from its inclusion in the sol gel, as we have been previously observed.<sup>11</sup> Further,  
38 comparison of SEM images of C-50 with and without PTA suggest that PTA also introduces pores  
39 into the composite (**Figures 3c-d**). This phenomenon is the result of PTA volatilization during  
40 carbonization and is known to increase not only surface area but also flexibility of CNFs and CNF  
41 composites.<sup>11, 34</sup>  
42  
43  
44  
45  
46  
47  
48  
49  
50

51 Unexpectedly, we also observed that PTA exerts a stabilizing effect on sol gel precursor  
52 suspensions containing P25. Higher mass loadings of P25, most notably C-80, could only be  
53 fabricated via electrospinning when PTA was present in precursor solutions at 2.5 wt.%, whereas  
54  
55  
56  
57  
58  
59  
60

1  
2  
3 similarly high mass loadings without PTA produced an unstable (i.e., aggregating and settling)  
4 precursor solution that could not be electrospun. Indeed, sedimentation studies conducted with P25  
5 nanoparticles suspended in DMF illustrate that inclusion of PTA results in a more stable sol gel  
6 suspension (**Figure S6**). We conclude, therefore, that PTA, an aromatic dicarboxylic acid, sorbs  
7 to the P25 surface in suspension, thereby functioning as a stabilizing ligand in DMF. In water,  
8 PTA is known to bind as a bidentate complex on  $\text{TiO}_2$ ,<sup>35</sup> and we presume a similar complex forms  
9 in polar DMF. Further, we propose that the ability of PTA to complex the P25 particle surface  
10 helps to promote the localization of macroporosity near the embedded P25 particles in the  
11 nanofiber composites; in fact, most pores observed in SEM images (see **Figure 3d**) are located  
12 near regions of the nanofibers where P25 is clearly concentrated.  
13  
14  
15  
16  
17  
18  
19  
20  
21  
22  
23  
24  
25

### 26 3.2. Optimization of C/TiO<sub>2</sub> reactivity

#### 27 3.2.1. Optimization of UV photocatalytic composite material properties

28  
29  
30 In the recirculating configuration, the reservoir atrazine concentration generally followed  
31 exponential decay with UV irradiation time in all experimental filtration systems (**Figure 4a**),  
32 behavior that was also observed for atrazine decay in closed (i.e., no flow) batch systems with  
33 suspended P25 nanoparticles (**Figure S7a**). This was the case both in UV-only controls (i.e., no  
34 C/TiO<sub>2</sub> composite filter) and in systems with C/TiO<sub>2</sub> filters across the range of P25 mass loadings  
35 investigated. We observed ~10% loss of atrazine through sorption to the C/TiO<sub>2</sub> filters (with the  
36 PVDF support) during the 1 h dark period prior to UV irradiation, and no additional atrazine loss  
37 via sorption occurred beyond 1 h suggesting sorption equilibrium was achieved. Moreover, UV  
38 light alone (i.e., in the absence of C/TiO<sub>2</sub> composites) photolyzed ~40% of atrazine over 3 h (the  
39 standard time period utilized in reactive filtration experiments).  
40  
41  
42  
43  
44  
45  
46  
47  
48  
49  
50  
51  
52  
53  
54  
55  
56  
57  
58  
59  
60



1  
2  
3 To compare reactivity across different C/TiO<sub>2</sub> filters, we calculated initial reaction rate  
4 coefficients (initial  $k_{\text{obs}}$  values) from the change in normalized atrazine concentration (i.e.,  
5 concentration at some time  $t$  divided by the initial concentration or  $C_t/C_0$ ) in the reservoir over UV  
6 irradiation time, assuming pseudo-first-order decay. Because some filtration systems exhibited  
7 deviations from pseudo-first-order decay over longer filter run times, we typically limited our  
8 kinetic analysis to reservoir concentrations measured over the first hour of filter operation. These  
9 initial  $k_{\text{obs}}$  values were then corrected to account for measured atrazine loss from direct UV  
10 photolysis.  
11  
12  
13  
14  
15  
16  
17  
18  
19  
20

21 Increasing the loading of P25 from 15 to 80 wt.% correspondingly increased the reactivity  
22 of C/TiO<sub>2</sub> nanofibers toward atrazine upon exposure to UV light (**Figure 4a**). Initial  $k_{\text{obs}}$  values  
23 increased from 0.004 to 0.013 min<sup>-1</sup> over this range, corresponding to half-lives from ~50 min to  
24 3 h. Assuming a steady-state concentration of hydroxyl radical ( $[\text{OH}^\bullet]_{\text{ss}}$ ) on or near the surface of  
25 the UV-irradiated filter, these coefficients correspond to concentrations between  $1 \times 10^{-12}$  to  $4 \times 10^{-12}$   
26 M. These values were estimated from our measured initial value of  $k_{\text{obs}} = k_{\text{OH}}[\text{OH}^\bullet]_{\text{ss}}$ , where  $k_{\text{OH}}$   
27 is the reported second order rate constant for atrazine oxidation by hydroxyl radical of  $3.17 \times 10^9$   
28 M<sup>-1</sup> s<sup>-1</sup> from Cooper *et al.*<sup>36</sup> Notably, C/TiO<sub>2</sub> exhibited roughly equivalent initial  $k_{\text{obs}}$  values in  
29 experiments with initial atrazine concentrations ranging from 0.14 μM (30 μg/L or ppb) up to ~1.5  
30 μM, supporting our use of a pseudo-first-order model to describe removal based on changes in  
31 reservoir concentration over time (**Figure S8**).  
32  
33  
34  
35  
36  
37  
38  
39  
40  
41  
42  
43  
44  
45  
46

47 Generally, initial  $k_{\text{obs}}$  values increased with P25 content, expressed both as bulk P25  
48 concentration (wt.%) and surface Ti concentration (at.%) from XPS (**Figure 4b-c**). This is  
49 consistent with the larger abundance of P25 in the composite nanofibers being able to produce a  
50 greater concentration of hydroxyl radical (and possibly other reactive oxygen species known to be  
51  
52  
53  
54  
55  
56  
57  
58  
59  
60

1  
2  
3 produced during P25 irradiation) at the nanofiber filter surface during UV irradiation. However,  
4 these correlations are not particularly strong, which may indicate that other physical and/or  
5 chemical factors influence atrazine degradation in these systems. For example, as P25 loading  
6 increases, so too does nanofiber diameter, which will influence the nominal pore size of the filter  
7 layer and potentially the degree of interaction between atrazine and the photocatalytic nanofiber  
8 surface.  
9

10  
11  
12 Based on the moderate reactivity, ease of fabrication, and handling ability of C-50, this  
13 material was selected to evaluate the influence of other synthetic variables on composite  
14 performance. For example, as shown in **Figure 4a**, the inclusion of PTA in C/TiO<sub>2</sub> had no impact  
15 on reactivity, while the use of 5 nm anatase TiO<sub>2</sub> in place of P25 rendered C/TiO<sub>2</sub> effectively  
16 unreactive as a photocatalyst (i.e., degradation of atrazine was on par with the UV control  
17 experiment without any TiO<sub>2</sub> material present) (**Figure S7b**). Complementary experiments  
18 conducted in batch compared the reactivity of unsupported 5 nm anatase particles to P25, showing  
19 that under UV irradiation P25 is roughly 3-fold more reactive than the pure anatase particles  
20 (**Figure S7a**). This inherent difference in reactivity relates to mixed phase TiO<sub>2</sub> (anatase and rutile)  
21 being recognized as a superior photocatalyst than either pure rutile or pure anatase because of an  
22 electron trapping mechanism associated with the mixed phases.<sup>37-38</sup> Nevertheless, from these batch  
23 suspension results, we would anticipate some increase in atrazine removal for composites prepared  
24 from 5 nm anatase particles. We assume that the lack of reactivity in these composites may reflect  
25 the greater extent of aggregation (and thus, lower degree of surface availability) for 5 nm particles  
26 relative to P25, both in precursor sol gel solutions and upon integration into nanofiber composites.  
27  
28  
29  
30  
31  
32  
33  
34  
35  
36  
37  
38  
39  
40  
41  
42  
43  
44  
45  
46  
47  
48  
49  
50  
51

52 As a final consideration, the performance of CNFs with embedded Au/TiO<sub>2</sub> particles was  
53 assessed. Despite clear increases in reactivity observed in closed batch systems for Au/TiO<sub>2</sub>  
54  
55  
56  
57  
58  
59  
60

1  
2  
3 relative to unmodified P25 particles (**Figure S9a**), no differences in reactivity were observed  
4  
5 during photocatalytic filtration studies with Au/TiO<sub>2</sub> containing CNF composites (**Figure S9b**).  
6  
7 We are left to assume that either the benefits of Au a co-catalyst are lost through the composite  
8  
9 fabrication process (e.g., during high temperature carbonization) or as a result of differences in the  
10  
11 rate-determining step of atrazine degradation in suspended Au/TiO<sub>2</sub> batch systems and flow  
12  
13 through systems with CNF supported Au/TiO<sub>2</sub> (e.g., surface reaction versus surface sorption  
14  
15 limited).  
16  
17  
18  
19

### 20 3.2.2. Optimization of photocatalytic filtration parameters

21  
22 Various flow rates in the recirculating cross-flow filtration system were assessed to  
23  
24 determine optimal conditions for removal of atrazine as a model organic pollutant (**Figure 5**).  
25  
26 During each run, atrazine concentrations were measured over time in the reservoir, retentate, and  
27  
28 permeate. This sampling regime allowed us to assess C-50 (electrospun with 2.5 wt% PTA) filter  
29  
30 performance in a recirculating cross-flow configuration by monitoring changes in reservoir  
31  
32 concentration over time. It also allowed us to evaluate the extent of atrazine removal in a single  
33  
34 pass through the irradiated filter by comparing the difference between the reservoir and permeate  
35  
36 concentrations at each sampling point.  
37  
38  
39

40  
41 Although the relatively high flow rates of 50 mL/min across and through the filter achieved  
42  
43 the fastest overall decrease in atrazine concentration in the reservoir (non-detect after 1.5 h), this  
44  
45 configuration benefited from high filter throughput to overcome relatively limited (~20%) removal  
46  
47 of atrazine with each pass through the UV-irradiated filter. In comparison, at flow rates of 10  
48  
49 mL/min across and through the filter, the reservoir concentration of atrazine reduced more  
50  
51 gradually (non-detect after 3 h) because of less volume being passed through the filter over time.  
52  
53 However, filter permeate immediately exhibited much lower concentrations of atrazine, achieving  
54  
55  
56  
57  
58  
59  
60

1  
2  
3 as much as 80% atrazine removal in a single pass. Indeed, the maximum atrazine removal achieved  
4  
5 in a single pass decreased considerably at higher flow rates (i.e., higher values of permeate flux)  
6  
7 (see **Figure 5d**), presumably because the contact time between the atrazine solution and the  
8  
9 irradiated C-50 filter layer is greatest at lower flux (estimated residence times in the ~600  $\mu\text{m}$  thick  
10  
11 filter layer were between approximately 1.2 and 6 for the highest and lowest flow rates,  
12  
13 respectively). So that we could continue to assess micropollutant removal in a single filter pass,  
14  
15 we conducted all additional experiments at this lower flow rate of 10 mL/min across and through  
16  
17 the filter.  
18  
19

20  
21 To minimize the amount of filter mass required for treatment, we also explored the  
22  
23 performance of C-50 nanofiber filters with half (~300  $\mu\text{m}$ ) and three-times (1800  $\mu\text{m}$ ) the thickness  
24  
25 of our standard recipe for composite filter fabrication (i.e., that used during previously discussed  
26  
27 optimization experiments; ~600  $\mu\text{m}$ ). At a flow rate of 10 mL/min, filters with cross-sectional  
28  
29 widths of  $290 \pm 20$ ,  $600 \pm 40$ , and  $1,800 \pm 200$   $\mu\text{m}$  as determined by SEM (corresponding to filter  
30  
31 residence times range from ~3 to 18 sec) all exhibited comparable reactivity toward atrazine  
32  
33 (**Figure S10**), with initial  $k_{\text{obs}}$  value estimated from reservoir atrazine concentrations of ~0.011  
34  
35  $\text{min}^{-1}$ . This suggests that the photoactive zone (i.e., the depth of the composite filter layer exposed  
36  
37 to light) is likely less than ~300  $\mu\text{m}$ , perhaps even considerably, such that any increases in filter  
38  
39 thickness beyond this depth provide little additional performance benefit. While we tried to explore  
40  
41 the performance of even thinner filter layers, composites thinner than ~300  $\mu\text{m}$  could not be  
42  
43 electrospun using our approach because the material was too thin to be removed from the collector  
44  
45 without damaging it. Due to its efficacy and the minimal amount of material needed to prepare  
46  
47 300  $\mu\text{m}$  thick filters (which corresponds to only ~30 mg of composite), this filter thickness was  
48  
49 used in all subsequent flow-through studies.  
50  
51  
52  
53  
54  
55  
56  
57  
58  
59  
60

1  
2  
3 Additional tests evaluated material performance during irradiation with wavelengths  
4 available in sunlight (using a 305 nm long-pass, cut-on filter). **Figure S11** compares the time-  
5 dependent removal of atrazine in a single filter pass (determined from the difference in reservoir  
6 and permeate concentration at each sampling point) for C-50 filters under UV and simulated  
7 sunlight. As expected UV light resulted in greater atrazine removal, but filters exposed to  
8 wavelengths of light greater than 305 nm were still able to remove between 20-50% of atrazine in  
9 a single pass. Notably, under both UV and >305 nm irradiation, the extent of atrazine removal in  
10 a single pass through the C-50 filter layer increased over time (see **Figure S11**). The timescales of  
11 our experiments should be sufficient to achieve steady-state  $\bullet\text{OH}$  production at or near the filter  
12 surface during irradiation, such that the available  $\bullet\text{OH}$  concentration should be reasonably constant  
13 over time. Instead, the increase in atrazine removal per filter pass over time likely reflects this  
14 near-constant level of  $\bullet\text{OH}$  reacting with a decreasing concentration of atrazine in the filter influent  
15 over time. Consistent with such a scenario, we observed near-constant removal of atrazine in a  
16 single pass through the filter (~40% loss compared to ~10% in dark controls) in a limited number  
17 of UV light experiments where the filtration system was operated without recirculation (i.e.,  
18 permeate was not returned to the feed reservoir; see **Figure S12**).

### 3.3. Performance of optimized nanofiber filters in environmentally relevant matrices and toward a suite of organic micropollutants

45 Filtration trials with atrazine in the presence of natural organic matter (10 mg/L Aldrich  
46 Humic Acid) and alkalinity (250 mg/L as  $\text{CaCO}_3$  at pH 9.5; typical conditions for tap water in our  
47 laboratory at the University of Iowa) revealed no influence on atrazine removal by C-50 filters  
48 (300  $\mu\text{m}$  thickness) over time in UV-irradiated systems (see **Figure S12**). Performance of these C-  
49 50 nanofiber filters was also assessed using recirculating, cross-flow UV-filtration (flow rates of  
50  
51  
52  
53  
54  
55  
56  
57  
58  
59  
60

1  
2  
3 10 mL/min across and through the filter) for the photochemical oxidation of solutions containing  
4 either 0.5  $\mu\text{M}$  atrazine, benzotriazole, caffeine, carbamazepine, DEET, metoprolol, naproxen or  
5 sulfamethoxazole. Normalized concentration profiles of each pollutant in the reservoir, retentate,  
6 and permeate, along with UV controls (without C-50 present), are shown in **Figure 6**. After  
7 equilibration for 1 h to allow for sorption,  $\sim 10\%$  of atrazine and  $\sim 15\%$  of DEET sorbed to filters,  
8 while all other compounds did not measurably sorb. Sulfamethoxazole was susceptible to direct  
9 photolysis, degrading by 80% over 3 h with exposure to UV light alone. Direct UV photolysis  
10 occurred to a lesser extent for atrazine ( $\sim 30\%$ ), benzotriazole (20%), caffeine (25%), DEET (20%),  
11 metoprolol (15%), and naproxen (30%) over a 3 h period, while carbamazepine was stable.  
12  
13  
14  
15  
16  
17  
18  
19  
20  
21  
22  
23

24 In the presence of C-50, the permeate had considerably reduced concentrations of each  
25 micropollutant as compared to the reservoir and retentate early in the trials (**Figure 6**). The notable  
26 decrease in sulfamethoxazole in retentate as compared to the reservoir was due to the impact of  
27 direct UV photolysis on concentration within the quartz filtration cell. Overall, the micropollutant  
28 suite exhibited half-lives [ $t_{1/2}$  values =  $\ln(2)/k_{\text{obs}}$ ] ranging from 45 min to 1 h in the recirculating  
29 flow through system, based on trends in reservoir concentration over time.  
30  
31  
32  
33  
34  
35  
36  
37

38 Using the difference at each sampling point between retentate and permeate concentration,  
39 **Figure S13** illustrates the time-dependent removal of each micropollutant in a single pass through  
40 the UV-irradiated C-50 filter. As observed earlier with atrazine (see **Figure S11**), the extent of  
41 removal in a single pass generally increases over time as micropollutant concentrations in the feed  
42 reservoir become depleted over time, in turn increasing the relative abundance of  $\bullet\text{OH}$  available at  
43 the filter surface to drive pollutant transformation. However, the extent of micropollutant removal  
44 in a single pass appears to stabilize between 60 to 90% across the analyte suite after  $\sim 30$  minutes  
45 of filter operation. We assume that pollutant removal in this regime becomes limited by the  
46  
47  
48  
49  
50  
51  
52  
53  
54  
55  
56  
57  
58  
59  
60

1  
2  
3 transport of the micropollutant to the near surface region of the irradiated C-50 filter where  $\bullet\text{OH}$   
4 concentrations are greatest. Indeed, initial  $k_{\text{obs}}$  values for micropollutant removal (from reservoir  
5 concentrations) do not appear to scale with reported second-order rate constants for the oxidation  
6 of each micropollutant with hydroxyl radical (i.e.,  $k_{\text{OH}}$  values)<sup>39</sup> (**Figure S14**). This likely implies  
7 that reaction with  $\bullet\text{OH}$  is not rate-limiting in the UV-irradiated filter system, and that other steps  
8 in the reaction sequence (e.g., micropollutant surface adsorption or product desorption) primarily  
9 control the overall rate of pollutant transformation in our system.

#### 20 **4. CONCLUSIONS AND ENVIRONMENTAL IMPLICATIONS**

21  
22 Herein, we optimize and evaluate the performance of photochemically reactive  
23  $\text{TiO}_2$ /carbon nanofibers, a stand-alone platform for use in applications where simultaneous  
24 filtration and chemical oxidation is desired. Electrospinning enabled a simple, single-pot synthesis  
25 of these photoactive composites, while stabilization and carbonization converted PAN, a polymer  
26 support susceptible to oxidative stress, into a more resistant carbon nanofiber ideal for advanced  
27 oxidation processes. The reactivity of C/ $\text{TiO}_2$  nanofiber filters was tunable and could be enhanced  
28 by increasing photocatalytic  $\text{TiO}_2$  loading within nanofibers (ultimately aided by inclusion of PTA  
29 as a stabilizing agent and porogen in electrospinning precursor solutions). An advantage of these  
30 filters is the relatively low mass of material required to achieve this level of treatment; optimal  
31 reactivity herein was obtained with only 30 mg of composite mass in a filter 0.3 mm thick.

32  
33 Addressing current and emerging challenges in water treatment, composite filters reveal  
34 relatively strong (60-90% removal in a single pass) performance toward a broad spectrum of  
35 organic micropollutants (atrazine, benzotriazole, caffeine, carbamazepine, DEET, metoprolol, and  
36 naproxen) generally known for their recalcitrance to more traditional forms of water treatment.  
37 We have also demonstrated the versatility of these materials across varying water quality (e.g.,  
38  
39  
40  
41  
42  
43  
44  
45  
46  
47  
48  
49  
50  
51  
52  
53  
54  
55  
56  
57  
58  
59  
60

1  
2  
3 NOM and alkalinity) and process flows, with high pollutant removal in a single pass akin to dead-  
4 end filtration at low flow rates or via a recirculating, cross-flow system at higher flows. Although  
5 not extensively investigated, for atrazine we also observed evidence (**Figure S15**) that  
6 transformation products can be subsequently degraded during recirculation, suggesting the  
7 potential to minimize formation of unwanted byproducts. We note that the extent of pollutant  
8 transformation achieved herein was accomplished at concentrations (500 nM) that are still high  
9 relative to typical values observed for micropollutants in sources used for drinking water (typically  
10 10's of ng/L to 100's of  $\mu\text{g/L}$ ). Our data suggest that a key factor in the extent of pollutant removal  
11 achieved in a single pass is the relative amount of photooxidants (e.g.,  $\bullet\text{OH}$ ) compared to the  
12 influent micropollutant concentration, where the rate of reaction with  $\bullet\text{OH}$  in the near-surface  
13 region is fast and does not appear to be rate-limiting. Thus, in systems with lower micropollutant  
14 concentrations, we would anticipate comparable, and perhaps even greater, degrees of removal in  
15 a single pass through the irradiated C/TiO<sub>2</sub> filter, although such assumptions need to be validated  
16 in systems with lower (e.g., ng/L) micropollutant concentrations and with micropollutant mixtures.

17  
18  
19 We anticipate that these findings will translate to systems beyond the bench scale testing  
20 apparatus used herein. Electrospinning is a mature fabrication route viable at industrial scales,<sup>40</sup>  
21 which should enable filter production for a range of applications in water treatment [from point-  
22 of-use and point-of-entry (POU/POE) to larger treatment systems]. In considering POU/POE  
23 applications, which are ideal for the small technology footprint of these nanofiber composites,  
24 results herein can be used to preliminarily assess the scale and performance of a treatment system  
25 used in home. Considering an influent with atrazine at a level 10-fold greater than the US EPA  
26 MCL (0.14  $\mu\text{M}$  or 30  $\mu\text{g/L}$ ),  $k_{\text{obs}}$  values measured herein can be used to estimate the amount of  
27 time needed to achieve safe drinking water with atrazine levels below the MCL. Using our  
28  
29  
30  
31  
32  
33  
34  
35  
36  
37  
38  
39  
40  
41  
42  
43  
44  
45  
46  
47  
48  
49  
50  
51  
52  
53  
54  
55  
56  
57  
58  
59  
60



1  
2  
3 standard 30 mg C-50 filter to treat 500 mL of water (or 0.06 g of C/TiO<sub>2</sub> per liter of water treated),  
4  
5 we estimate a clean water production rate of 0.13 L/h. Furthermore, if the average consumer drinks  
6  
7 2 L of water of day, it would only take ~44 grams (or ~0.01 lbs.) of C/TiO<sub>2</sub> per year to treat an  
8  
9 individual's water supply to a safe level of atrazine at this production rate. Of course, a larger  
10  
11 filtration system using more mass of C/TiO<sub>2</sub> per liter of water would increase the clean water  
12  
13 production rate of such a POU/POE system. We find these estimates encouraging, although  
14  
15 certainly more work is needed to produce C/TiO<sub>2</sub> nanofibers at the scale necessary to validate the  
16  
17 performance of such a photoactive treatment system. Assuming a suitable photoreactive filtration  
18  
19 design can be developed, the performance of C/TiO<sub>2</sub> and its stability over longer application run  
20  
21 times more typical of an individual's water treatment needs (i.e., over days to years) will also need  
22  
23 to be validated at deployment scale.  
24  
25  
26  
27  
28  
29

## 30 31 **5. ACKNOWLEDGEMENTS**

32  
33 This work was supported by the U.S. EPA (grant number R835177) and by NSF 1804757  
34  
35 and 2040464. K.E.G. was supported by a University of Iowa (UI) Presidential Graduate Research  
36  
37 Fellowship and through funding from the Donald E. Bently Professorship at UI.  
38  
39  
40  
41  
42  
43  
44  
45  
46  
47  
48  
49  
50  
51  
52  
53  
54  
55  
56  
57  
58  
59  
60

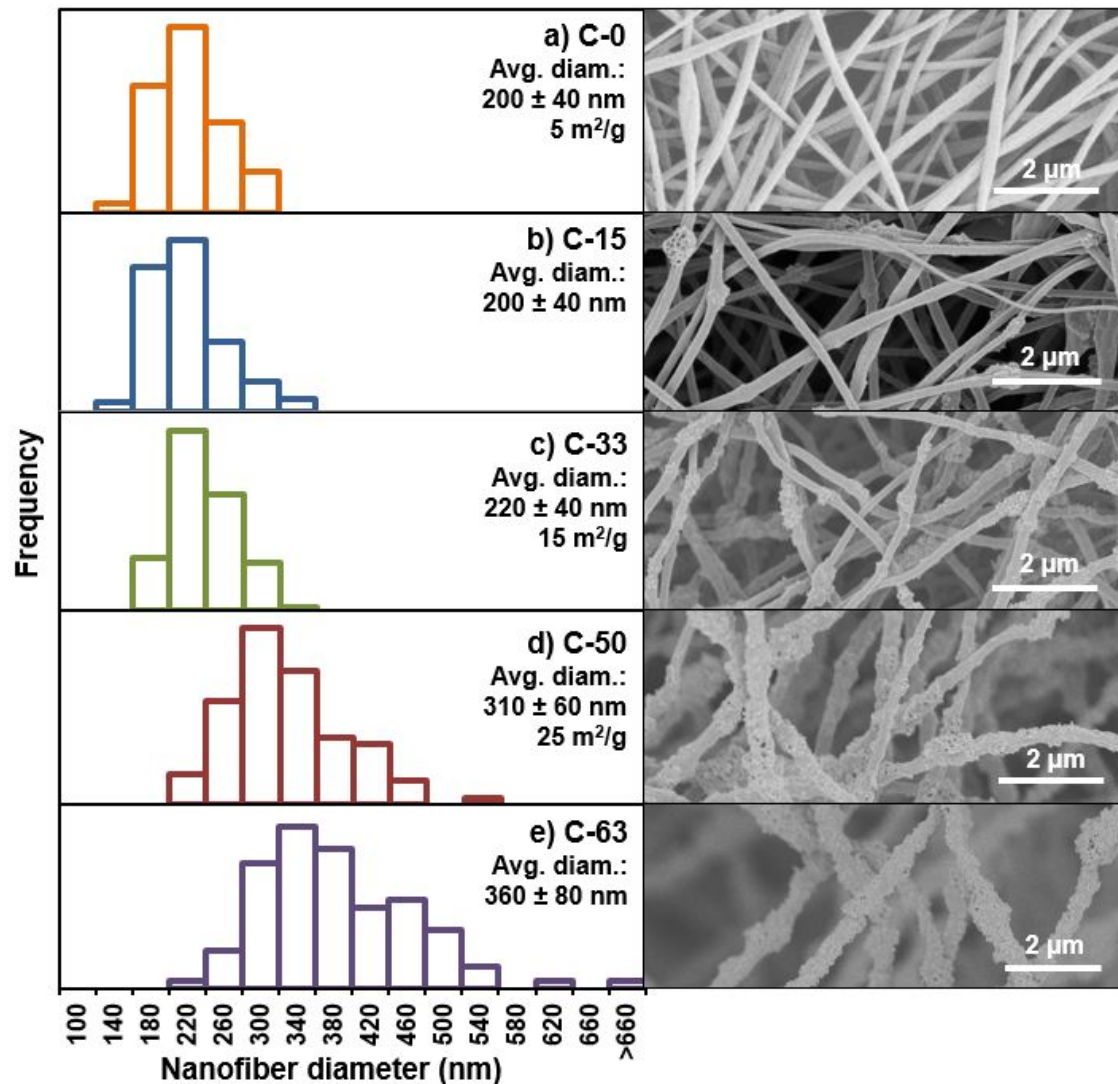


**Figure 1.** Histograms and associated SEM images for (a) C-0 (0 wt.% P25), (b) C-15, (c) C-33, (d) C-50, and (e) C-63 nanofiber composites. All electrospun sol gels contained 2.5 wt.% PTA. As mass loading of P25 in the nanofibers increased, nanofibers transitioned from smooth carbon nanofibers, to rough nanofibers with visible TiO<sub>2</sub> aggregates and increased surface area.

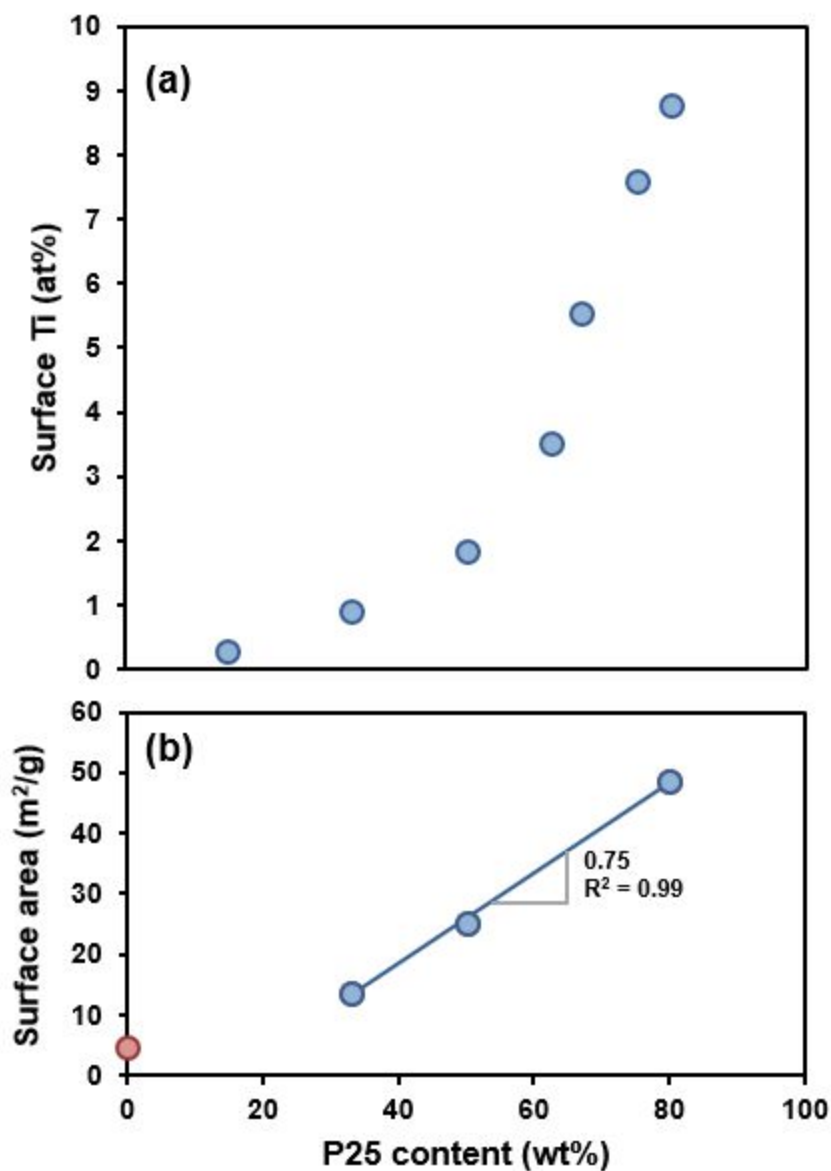


**Figure 2.** (a) Surface concentration of Ti (atom % determined via XPS) and (b) surface area of C/TiO<sub>2</sub> nanofiber composites as function of P25 content in the nanofibers. Above 63 wt.% P25, increases in P25 corresponded with sharp increase in surface Ti. Surface area increased linearly between 33 wt.% P25 and 80 wt.% mass loadings in nanofibers.

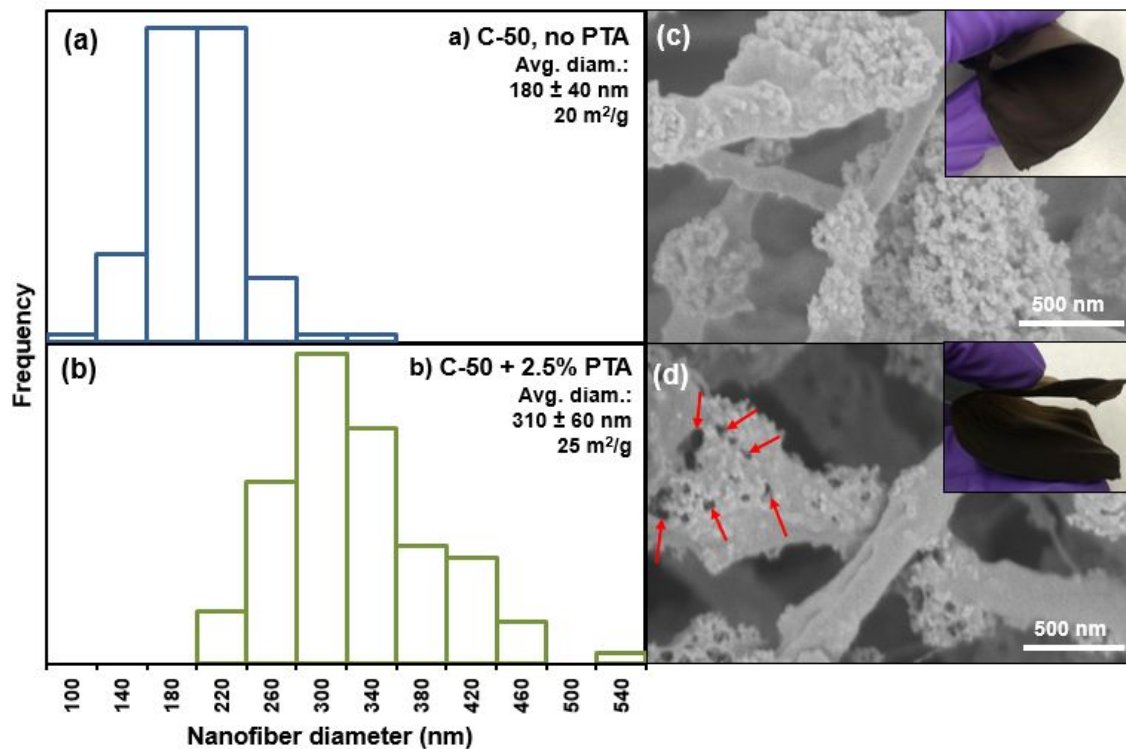


**Figure 3.** Histograms, SEM images, and digital images of (a,c) C-50 without PTA and (b,c) C-50 with 2.5 wt.% PTA. Pores introduced into nanofibers via PTA inclusion are indicated with red arrows in (d). Both materials remained flexible after stabilization/carbonization (c,d).

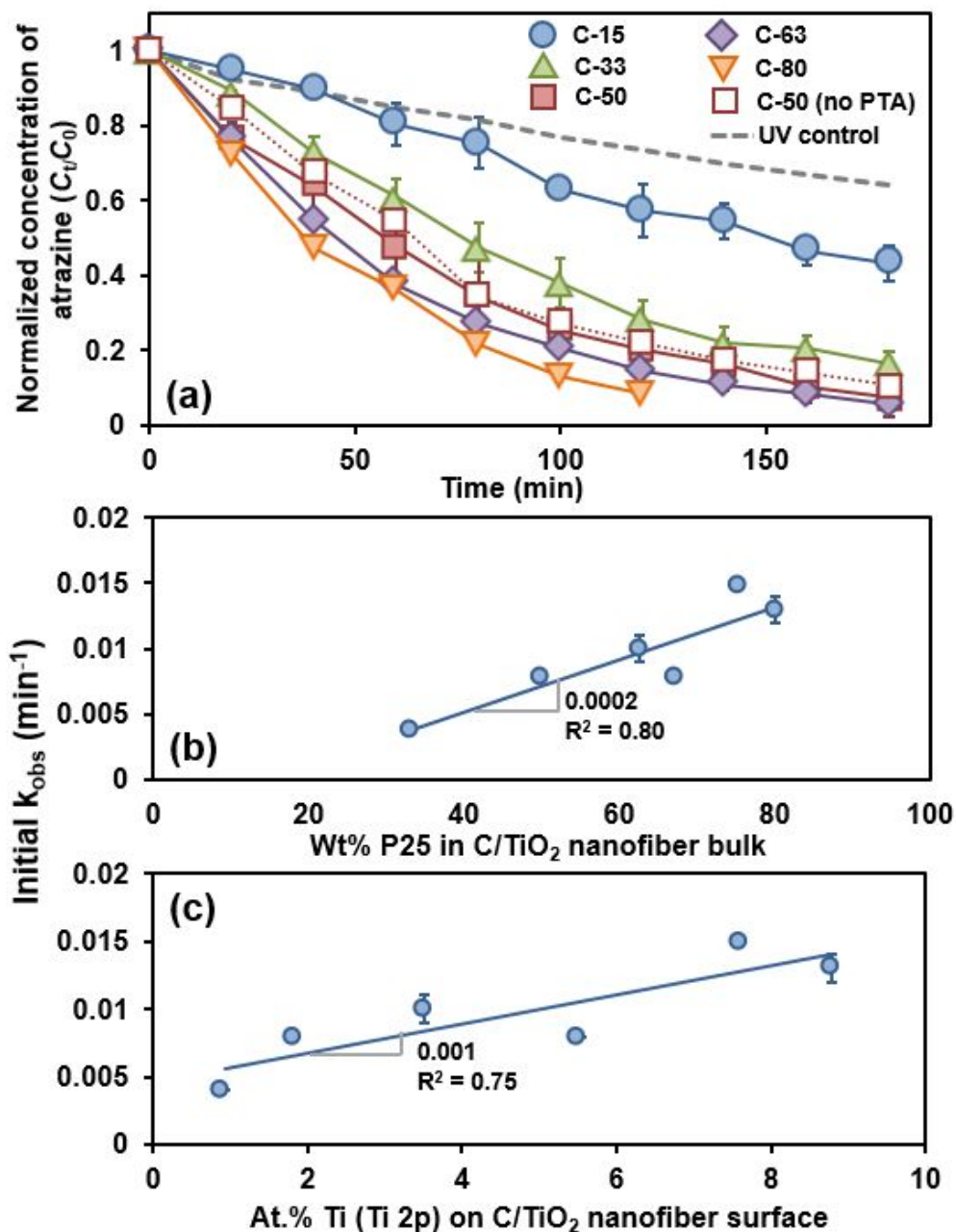


**Figure 4.** (a) Curves showing phototransformation of 30  $\mu\text{g/L}$  atrazine over time for C/TiO<sub>2</sub> nanofiber composites with different mass loadings of P25 (15 to 80 wt.%), with and without PTA. A UV control (conducted without TiO<sub>2</sub> material) is shown with the grey dashed line. (b) Observed initial rate constants ( $k_{obs}$ ) as a function of P25 content of nanofibers, and (c) initial  $k_{obs}$  as a function of resultant surface Ti abundance

1  
2  
3  
4 determined via XPS. Rate coefficients correspondingly increased with increasing bulk  
5 and surface TiO<sub>2</sub>.  
6  
7  
8  
9  
10  
11  
12  
13  
14  
15  
16  
17  
18  
19  
20  
21  
22  
23  
24  
25  
26  
27  
28  
29  
30  
31  
32  
33  
34  
35  
36  
37  
38  
39  
40  
41  
42  
43  
44  
45  
46  
47  
48  
49  
50  
51  
52  
53  
54  
55  
56  
57  
58  
59  
60

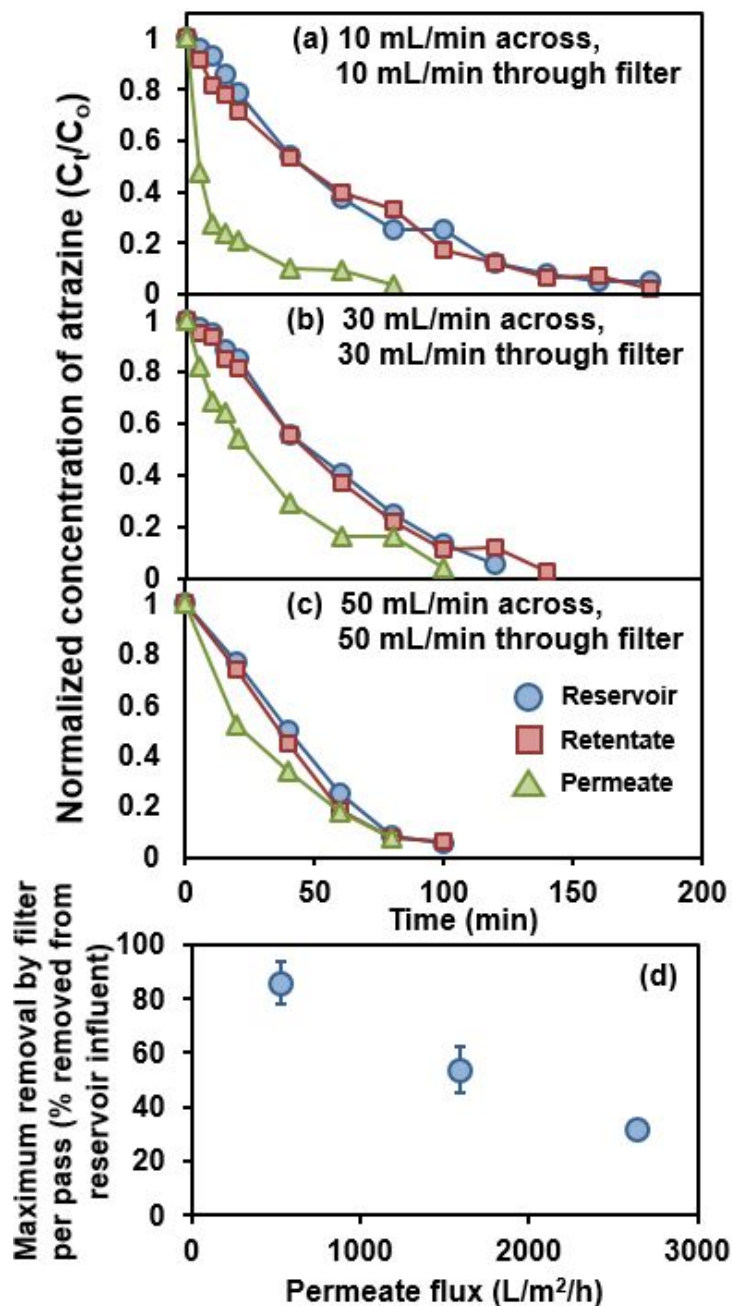


**Figure 5.** Normalized concentration of atrazine (with initial  $30 \mu\text{g/L}$  concentration) over time in cross-flow filtration reservoir, retentate, and permeate for (a) 10 mL/min retentate and permeate flow rates, (b) 30 mL/min retentate and permeate flow rates, and (c) 50 mL/min retentate and permeate flow rates. Although more removal is achieved overall with high flow rates (c), low flow rates correspond with more removal of influent to the filter [as measured by permeate concentrations (a)]. (d) Maximum

1  
2  
3  
4 removal of atrazine by filter pass (determine from differences in concentration between  
5 filter influent and permeate at each time point) across permeate fluxes. Only 540 L/m<sup>2</sup>/h,  
6 the leftmost point with the highest maximum removal, falls within the range of  
7  
8  
9 microfiltration.  
10  
11  
12  
13  
14  
15  
16  
17  
18  
19  
20  
21  
22  
23  
24  
25  
26  
27  
28  
29  
30  
31  
32  
33  
34  
35  
36  
37  
38  
39  
40  
41  
42  
43  
44  
45  
46  
47  
48  
49  
50  
51  
52  
53  
54  
55  
56  
57  
58  
59  
60



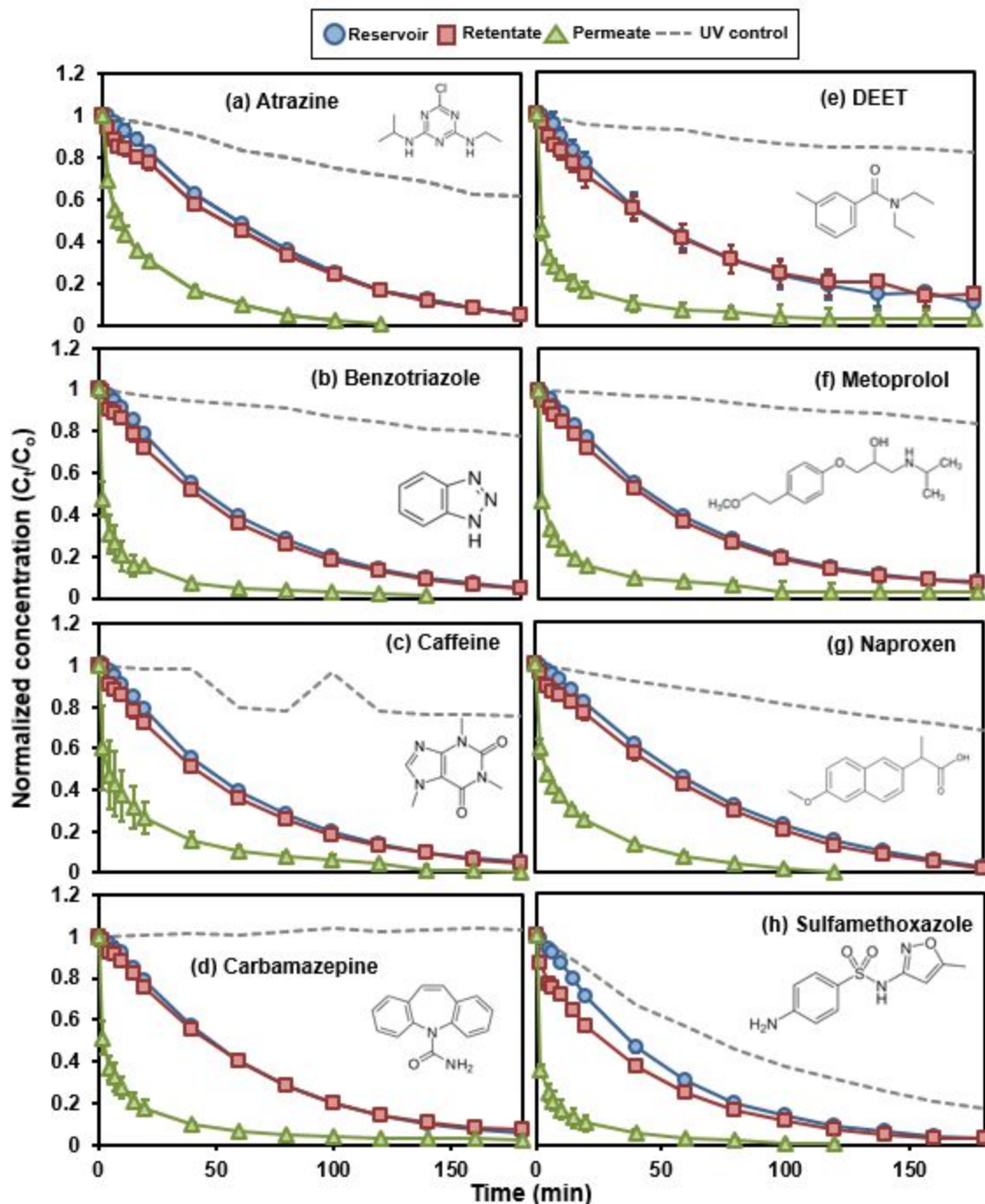


**Figure 6.** Normalized concentration chemical contaminants over time in cross-flow filtration reservoir, retentate, and permeate with initial  $0.5 \mu\text{M}$  (a) atrazine, (b) benzotriazole, (c) caffeine, (d) carbamazepine, (e) DEET, (f) metoprolol, (g) naproxen, and (h) sulfamethoxazole. UV controls, conducted without  $\text{TiO}_2$  material present, are shown by grey dashed lines.

## 6. REFERENCES

1. Eslami, A.; Amini, M. M.; Asadi, A.; Safari, A. A.; Daglioglu, N., Photocatalytic degradation of ibuprofen and naproxen in water over NS-TiO<sub>2</sub> coating on polycarbonate: Process modeling and intermediates identification. *Inorganic Chemistry Communications* **2020**, *115*, 107888.
2. Nguyen, A. T.; Juang, R.-S., Treatment of o-Cresol/4-chlorophenol binary mixtures in aqueous solutions by TiO<sub>2</sub> photocatalysis under UV irradiation. *Desalination and Water Treatment* **2016**, *57* (15), 6820-6828.
3. Zhao, Z.; Wang, Y.; Xu, J.; Wang, Y., Mesoporous Ag/TiO<sub>2</sub> nanocomposites with greatly enhanced photocatalytic performance towards degradation of methyl orange under visible light. *RSC Advances* **2015**, *5* (73), 59297-59305.
4. Loeb, S. K.; Alvarez, P. J. J.; Brame, J. A.; Cates, E. L.; Choi, W.; Crittenden, J.; Dionysiou, D. D.; Li, Q.; Li-Puma, G.; Quan, X.; Sedlak, D. L.; David Waite, T.; Westerhoff, P.; Kim, J.-H., The Technology Horizon for Photocatalytic Water Treatment: Sunrise or Sunset? *Environ. Sci. Technol.* **2019**, *53* (6), 2937-2947.
5. Wiesner, M. R.; Lowry, G. V.; Alvarez, P.; Dionysiou, D.; Biswas, P., Assessing the risks of manufactured nanomaterials. *Environ. Sci. Technol.* **2006**, *40* (14), 4336-45.
6. Zhang, Y.; Chen, Y.; Westerhoff, P.; Hristovski, K.; Crittenden, J. C., Stability of commercial metal oxide nanoparticles in water. *Water Research* **2008**, *42* (8), 2204-2212.
7. Nalbandian, M. J.; Greenstein, K. E.; Shuai, D.; Zhang, M.; Choa, Y.-H.; Parkin, G. F.; Myung, N. V.; Cwiertny, D. M., Tailored Synthesis of Photoactive TiO<sub>2</sub> Nanofibers and Au/TiO<sub>2</sub> Nanofiber Composites: Structure and Reactivity Optimization for Water Treatment Applications. *Environ. Sci. Technol.* **2015**, *49* (3), 1654-1663.
8. Greenstein, K. E.; Myung, N. V.; Parkin, G. F.; Cwiertny, D. M., Performance comparison of hematite ( $\alpha$ -Fe<sub>2</sub>O<sub>3</sub>)-polymer composite and core-shell nanofibers as point-of-use filtration platforms for metal sequestration. *Water Research* **2019**, *148*, 492-503.
9. Sun, C.; Wang, N.; Zhou, S.; Hu, X.; Zhou, S.; Chen, P., Preparation of self-supporting hierarchical nanostructured anatase/rutile composite TiO<sub>2</sub> film. *Chemical Communications* **2008**, (28), 3293-3295.
10. Qian, J.; Jennings, B.; Cwiertny, D. M.; Martinez, A., Emerging investigator series: development and application of polymeric electrospun nanofiber mats as equilibrium-passive sampler media for organic compounds. *Environ. Sci. Process. Impacts* **2017**, *19* (11), 1445-1456.
11. Peter, K. T.; Vargo, J. D.; Rupasinghe, T. P.; De Jesus, A.; Tivanski, A. V.; Sander, E. A.; Myung, N. V.; Cwiertny, D. M., Synthesis, Optimization, and Performance Demonstration of Electrospun Carbon Nanofiber–Carbon Nanotube Composite Sorbents for Point-of-Use Water Treatment. *ACS Applied Materials & Interfaces* **2016**, *8* (18), 11431-11440.
12. Lee, C.-G.; Javed, H.; Zhang, D.; Kim, J.-H.; Westerhoff, P.; Li, Q.; Alvarez, P. J. J., Porous Electrospun Fibers Embedding TiO<sub>2</sub> for Adsorption and Photocatalytic Degradation of Water Pollutants. *Environ. Sci. Technol.* **2018**, *52* (7), 4285-4293.

13. Deniz, A. E.; Celebioglu, A.; Kayaci, F.; Uyar, T., Electrospun polymeric nanofibrous composites containing TiO<sub>2</sub> short nanofibers. *Materials Chemistry and Physics* **2011**, *129* (3), 701-704.
14. Im, J. S.; Kim, M. I.; Lee, Y.-S., Preparation of PAN-based electrospun nanofiber webs containing TiO<sub>2</sub> for photocatalytic degradation. *Materials Letters* **2008**, *62* (21), 3652-3655.
15. Lombardi, M.; Palmero, P.; Sangermano, M.; Varesano, A., Electrospun polyamide-6 membranes containing titanium dioxide as photocatalyst. *Polymer International* **2011**, *60* (2), 234-239.
16. Hong, Y.; Li, D.; Zheng, J.; Zou, G., Sol-gel growth of titania from electrospun polyacrylonitrile nanofibres. *Nanotechnology* **2006**, *17* (8), 1986-1993.
17. Mehrpouya, F.; Tavanai, H.; Morshed, M.; Ghiaci, M., The formation of titanium dioxide crystallite nanoparticles during activation of PAN nanofibers containing titanium isopropoxide. *Journal of Nanoparticle Research* **2012**, *14* (8), 1074.
18. Meng, X.; Luo, N.; Cao, S.; Zhang, S.; Yang, M.; Hu, X., In-situ growth of titania nanoparticles in electrospun polymer nanofibers at low temperature. *Materials Letters* **2009**, *63* (16), 1401-1403.
19. Su, C.; Tong, Y.; Zhang, M.; Zhang, Y.; Shao, C., TiO<sub>2</sub> nanoparticles immobilized on polyacrylonitrile nanofibers mats: a flexible and recyclable photocatalyst for phenol degradation. *RSC Advances* **2013**, *3* (20), 7503-7512.
20. Abdal-hay, A.; Mousa, H. M.; Khan, A.; Vanegas, P.; Lim, J. H., TiO<sub>2</sub> nanorods coated onto nylon 6 nanofibers using hydrothermal treatment with improved mechanical properties. *Colloids and Surfaces A: Physicochemical and Engineering Aspects* **2014**, *457*, 275-281.
21. Szatmáry, L.; Šubrt, J.; Kalousek, V.; Mosinger, J.; Lang, K., Low-temperature deposition of anatase on nanofiber materials for photocatalytic NO<sub>x</sub> removal. *Catalysis Today* **2014**, *230*, 74-78.
22. Zhang, H.; Yang, L., Immobilization of nanoparticle titanium dioxide membrane on polyamide fabric by low temperature hydrothermal method. *Thin Solid Films* **2012**, *520* (18), 5922-5927.
23. Kim, S.; Lim, S. K., Preparation of TiO<sub>2</sub>-embedded carbon nanofibers and their photocatalytic activity in the oxidation of gaseous acetaldehyde. *Applied Catalysis B: Environmental* **2008**, *84* (1), 16-20.
24. Su, C.; Ran, X.; Hu, J.; Shao, C., Photocatalytic Process of Simultaneous Desulfurization and Denitrification of Flue Gas by TiO<sub>2</sub>-Polyacrylonitrile Nanofibers. *Environmental Science & Technology* **2013**, *47* (20), 11562-11568.
25. Tai, M. H.; Gao, P.; Tan, B. Y. L.; Sun, D. D.; Leckie, J. O., A Hierarchically-Nano Structured TiO<sub>2</sub>-Carbon Nanofibrous Membrane for Concurrent Gravity-Driven Oil-Water Separation. *Int. J. Environ. Sci. Dev.* **2015**, *6* (8), 590-595.
26. Ramasundaram, S.; Son, A.; Seid, M. G.; Shim, S.; Lee, S. H.; Chung, Y. C.; Lee, C.; Lee, J.; Hong, S. W., Photocatalytic applications of paper-like poly(vinylidene fluoride)-

- 1  
2  
3 titanium dioxide hybrids fabricated using a combination of electrospinning and  
4 electrospaying. *Journal of hazardous materials* **2015**, *285*, 267-76.  
5  
6 27. Memetea, L. T.; Billingham, N. C.; Then, E. T. H., Hydroperoxides in polyacrylonitrile  
7 and their role in carbon-fibre formation. *Polymer Degradation and Stability* **1995**, *47* (2),  
8 189-201.  
9  
10 28. Gu, Y.; Li, C.; Bai, J.; Wang, J.; Ma, T., One-step solvothermal synthesis of Au-TiO<sub>2</sub>  
11 loaded electrospun carbon fibers to enhance photocatalytic activity. *Vacuum* **2016**, *130*, 1-  
12 6.  
13  
14 29. Kim, C. H.; Kim, B.-H.; Yang, K. S., TiO<sub>2</sub> nanoparticles loaded on graphene/carbon  
15 composite nanofibers by electrospinning for increased photocatalysis. *Carbon* **2012**, *50*  
16 (7), 2472-2481.  
17  
18 30. Melcher, J.; Feroz, S.; Bahnemann, D., Comparing photocatalytic activities of  
19 commercially available iron-doped and iron-undoped aerioxide TiO<sub>2</sub> P25 powders. *Journal*  
20 *of Materials Science* **2017**, *52* (11), 6341-6348.  
21  
22 31. Benotti, M. J.; Trenholm, R. A.; Vanderford, B. J.; Holady, J. C.; Stanford, B. D.; Snyder,  
23 S. A., Pharmaceuticals and Endocrine Disrupting Compounds in U.S. Drinking Water.  
24 *Environ. Sci. Technol.* **2009**, *43* (3), 597-603.  
25  
26 32. Oulton, R. L.; Kohn, T.; Cwiertny, D. M., Pharmaceuticals and personal care products in  
27 effluent matrices: A survey of transformation and removal during wastewater treatment  
28 and implications for wastewater management. *J. Environ. Monit.* **2010**, *12* (11), 1956-78.  
29  
30 33. Westerhoff, P.; Yoon, Y.; Snyder, S.; Wert, E., Fate of Endocrine-Disruptor,  
31 Pharmaceutical, and Personal Care Product Chemicals during Simulated Drinking Water  
32 Treatment Processes. *Environ. Sci. Technol.* **2005**, *39* (17), 6649-6663.  
33  
34 34. Liu, H.; Cao, C.-Y.; Wei, F.-F.; Huang, P.-P.; Sun, Y.-B.; Jiang, L.; Song, W.-G., Flexible  
35 macroporous carbon nanofiber film with high oil adsorption capacity. *Journal of Materials*  
36 *Chemistry A* **2014**, *2* (10), 3557-3562.  
37  
38 35. Dobson, K. D.; McQuillan, A. J., In situ infrared spectroscopic analysis of the adsorption  
39 of aromatic carboxylic acids to TiO<sub>2</sub>, ZrO<sub>2</sub>, Al<sub>2</sub>O<sub>3</sub>, and Ta<sub>2</sub>O<sub>5</sub> from aqueous solutions.  
40 *Spectrochimica Acta Part A: Molecular and Biomolecular Spectroscopy* **2000**, *56* (3), 557-  
41 565.  
42  
43 36. Cooper, W. J.; Snyder, S. A.; Mezyk, S. P.; Peller, J. R.; Nickelsen, M. G. Reaction Rates  
44 and Mechanisms of Advanced Oxidation Processes (AOPs) for Water Reuse. Project  
45 Report 04-17. Water Reuse Foundation, 2010. Available at:  
46 [https://watereuse.org/watereuse-research/04-17-reaction-rates-and-mechanisms-of-](https://watereuse.org/watereuse-research/04-17-reaction-rates-and-mechanisms-of-advanced-oxidation-processes-aops-for-water-reuse/)  
47 [advanced-oxidation-processes-aops-for-water-reuse/](https://watereuse.org/watereuse-research/04-17-reaction-rates-and-mechanisms-of-advanced-oxidation-processes-aops-for-water-reuse/)  
48  
49 37. Hurum, D. C.; Agrios, A. G.; Gray, K. A.; Rajh, T.; Thurnauer, M. C., Explaining the  
50 Enhanced Photocatalytic Activity of Degussa P25 Mixed-Phase TiO<sub>2</sub> Using EPR. *The*  
51 *Journal of Physical Chemistry B* **2003**, *107* (19), 4545-4549.  
52  
53 38. Scanlon, D. O.; Dunnill, C. W.; Buckeridge, J.; Shevlin, S. A.; Logsdail, A. J.; Woodley,  
54 S. M.; Catlow, C. R. A.; Powell, M. J.; Palgrave, R. G.; Parkin, I. P.; Watson, G. W.; Keal,  
55  
56  
57  
58  
59  
60

- 1  
2  
3 T. W.; Sherwood, P.; Walsh, A.; Sokol, A. A., Band Alignment of Rutile and Anatase TiO<sub>2</sub>.  
4 *Nature Materials* **2013**, *12* (9), 798-801.  
5  
6 39. Mandal, S., Reaction Rate Constants of Hydroxyl Radicals with Micropollutants and Their  
7 Significance in Advanced Oxidation Processes. *J. Adv. Oxid. Technol.* **2018**, *21* (1), doi:  
8 10.26802/jaots.2017.0075.  
9  
10 40. Persano, L.; Camposeo, A.; Tekmen, C.; Pisignano, D., Industrial Upscaling of  
11 Electrospinning and Applications of Polymer Nanofibers: A Review. *Macromolecular*  
12 *Materials and Engineering* **2013**, *298* (5), 504-520.  
13  
14  
15  
16  
17  
18  
19  
20  
21  
22  
23  
24  
25  
26  
27  
28  
29  
30  
31  
32  
33  
34  
35  
36  
37  
38  
39  
40  
41  
42  
43  
44  
45  
46  
47  
48  
49  
50  
51  
52  
53  
54  
55  
56  
57  
58  
59  
60